Electronic Supplementary Material (ESI) for Energy & Environmental Science.

Supplemental Information: Insights into Operational Stability and Processing of Halide Perovskite Active Layers

Laura T. Schelhas[1], Zhen Li[2,3], Jeffrey A. Christians[2,4], Anuj Goyal[5], Paul Kairys[5], Steven Harvey[2], Dong Hoe Kim[2], Kevin H. Stone[1], Joseph M. Luther[2], Kai Zhu[2], Vladan Stevanovic[5], Joseph J. Berry[2]

[1] SLAC National Accelerator Laboratory, Menlo Park, California 94025, United States.
[2] National Renewable Energy Laboratory, Golden, CO, 80401, United States.
[3] State Key Laboratory of Solidification Processing, Center for Nano Energy Materials, School of Materials Science and Engineering, Northwestern Polytechnical University and Shaanxi Joint Laboratory of Graphene (NPU), Xi'an, 710072, P. R. China.
[4] Hope College, Holland, MI 49423, United States.
[5] Colorado School of Mines, Golden, CO, 80401, United States

**Current address: State Key Laboratory of Solidification Processing, Center for Nano Energy Materials, School of Materials Science and Engineering, Northwestern Polytechnical University and Shaanxi Joint Laboratory of Graphene (NPU), Xi'an, 710072, P. R. China*

Experimental Methods:

Materials. Methylammonium iodide (CH_3NH_3I, MAI), and formamidinium iodide ($CH(NH_2)_2$, FAI) were purchased from Dyesol. Lead (II) iodide (99.9985% metals basis) was purchased from Alfa Aesar. 2,2',7,7'-tetrakis(N,N-di-p-methoxyphenylamino)-9,9'-spirobifluorene (spiro-OMeTAD) was purchased from Lumtec. All other chemicals were purchased from Sigma-Aldrich and used as received.

Perovskite Active Layers. The precursor for the $FA_{0.85}Cs_{0.15}PbI_3$ (FA-Cs) perovskite active layers was prepared by dissolving 461 mg of PbI_2, 39.0 mg CsI and 146.2 mg FAI in 1 mL of DMF/DMSO mixed solvents (v/v=7:3). The precursors were stirred for 2 h to obtain a clear yellow-color solution. The precursor solution was filtered through a PTFE filter (0.2 μm) before use. The FA-Cs thin film was deposited by a 3-step spin-coating process, with 100 rpm for 5 s, 3000 rpm for 10 s and 5000 rpm for 30 s. With 10 s remaining in the final step about 1 mL of toluene was dispersed on the spinning substrate to remove excess DMF/DMSO solvents. The films were annealed at 170 ^oC for 15 min.

The precursor for the $FA_{0.758}MA_{0.152}Cs_{0.091}PbI_3$ (FA-MA-Cs) perovskite active layers were prepared by dissolving 600 mg PbI_2, 31.8 mg MAI, and 172 mg FAI in 1 mL of DMF/DMSO mixed solvents (v/v=4:1). Then 80 μL of a 1.5 M stock solution of CsI in DMSO was added to the solution and the precursors were stirred until a clear yellow-color solution was obtained. The FA-MA-Cs thin films were deposited by spin-coating with a 2-step process with 1000 rpm for 10 s, followed by 6000 rpm for 20 s. With 6 s remaining in the final step about 100 μL of chlorobenzene was dispersed on the spinning substrate. The films were annealed at 100 °C for 1 hr.

***Device Fabrication*.** An approximately 30 nm TiO_2 compact layer was deposited on cleaned, patterned fluorine-doped tin oxide (FTO) glass substrates by spray pyrolysis at 450 °C. The perovskite active layer was deposited on the TiO_2 layer in a nitrogen flow box as described above. Following annealing of the perovskite layer, a spiro-OMeTAD hole transport layer was deposited by spin-coating at 4000 rpm for 30 s. The spiro-OMeTAD solution consisted of 72 mg spiro-OMeTAD, 17.5 µL LiTFSI stock solution (520 mg/mL LiTFSI in acetonitrile), and 28.8 µL 4-tert-butylpyridine. The films were then stored in dry air overnight and completed by evaporation of a 100 nm Au contact.

Devices used in the stability experiments shown in Fig. S9 were prepared as follows. The ITO glass was cleaned by the same procedure outlined for FTO glass. An aqueous SnO_2 colloid solution, obtained from Alfa Aesar (Tin(IV) oxide, 15% in H_2O colloidal dispersion) , was diluted 1:6.5 v/v with deionized water, and spin cast at 3000 rpm for 30 s. The SnO_2 films were then dried at 150 °C for 30 min and cleaned for 15 min by UV-ozone immediately before use.

***Ex-situ Device Characterization*.** Solar cell performance was measured under 100 mW/cm^2 simulated AM 1.5G illumination with an Oriel Sol3A solar simulator which was calibrated with an NREL-certified Si reference solar cell. The current density-voltage (*J-V*) measurements were contacted using a Keithley 2400 source meter. Device stability tests in the absence of X-ray exposure were conducted under ISOS-L1 conditions: constant illumination, fixed 550 Ω load resistance, and an ambient environment.

In-situ X-ray Characterization. X-ray diffraction data was collected at the Stanford synchrotron radiation light source (SSRL). To determine the effect operation has on the structural stability of mixed A-site PSCs devices were measured within a custom built chamber (Figure SX).[1] IV/XRD measurements are collected in this climate controlled chamber with relative humidity of ~50%. The samples are illuminated using approximately 1-sun intensity from an Asahi Spectra Hal-320 Solar Simulator and *I-V* curves (forward and reverse) are collected, followed by a XRD scan, this cycle is repeated every 15 minutes. Samples were measured in the flat plate geometry with the beam position aligned to measure through the operating top Au electrode. The data were taken using the Pilatus 100K small area detector and calibrated using an Al_2O_3 standard. The samples were measured at an incidence angle of 2° with incident X-ray energy of 12.5 keV and the flux was approximately 4.9×1010 photon $s^{-1}mm^{-2}$ with 30 secs of X-ray exposure per scan.

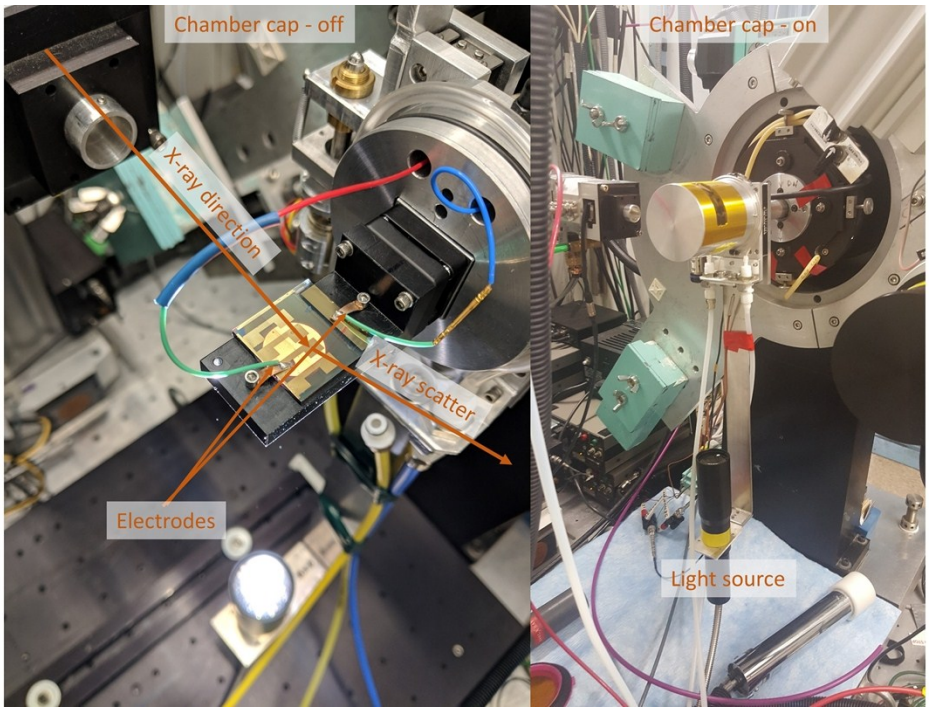

Figure S1. Photos of the chamber used at SSRL. This chamber allows for electrical contact to the device by small clips shown on the left. The light is applied from the bottom of the chamber and the X-ray spot is focused on the operational pad. Gas inlet/outlet ports allow for environmental control.[1]

Temperature dependent X-ray diffraction data (Figure 4) were collected on SSRL BL11-3 at a heating rate of 2°C/3 min and an X-ray wavelength of 0.9744 Å. Two-dimensional scattering data were collected using a Rayonex MX225 detector in a grazing incidence geometry with the X-ray beam held at an incident angle of 3°. Diffraction data were collected with a 30 second exposure time per scan in a sealed chamber under helium flow. Images were calibrated using a LaB_6 standard and integrated between $10° < \chi < 170°$ (χ is the polar angle) using GSAS-II.[2]

Ex-situ X-ray Characterization

To confirm the reproducibility of the synchrotron based X-ray experiments, devices were characterized *ex situ* (see above "*Ex-situ* device characterization). After the stability tests XRD of the perovskite films were measured using an X-ray diffractometer (Rigaku D-Max 2200) with Cu Kα radiation.

TOF-SIMS. An ION-TOF TOF-SIMS V Time of Flight SIMS (TOF-SIMS) spectrometer was utilized for chemical imaging of the perovskite utilizing methods outlined in detail by Harvey *et.al*.[3] Analysis was completed utilizing a 3-lens 30kV BiMn primary ion gun. Imaging was completed with 100nm lateral resolution using a Bi_3^{++} primary ion-beam cluster (100ns pulse width, 0.1pA pulsed beam current), a 50x50 µm area was sampled with a 1024:1024 primary beam raster. Prior to imaging sputter cleaning of the surface was accomplished with a 1kV oxygen ion sputter beam (2 nA sputter current) with a raster of 150×150 microns. The images as shown were

subjected to a center-weighted pixel averaging treatment, considering only the 8 first nearest neighboring pixels around each pixel.

Theory.

Modeling mixed A-site halide perovskites. Mixed A-site halide perovskites structures are created using pseudo-cubic as the starting structure for the pure compositions (obtained from C. C. Stoumpos et al.[4]) with random substitution at the A-site. Structures for various A-site compositions are generated using the special quasi-random structure (SQS) method[5] as implemented in the ATAT package.[6,7] Supercell sizes of 96 and 144-atoms are used for SQS structures and for each A-site composition multiple structures, varying in the orientation of the FA and MA molecule, are considered. The DFT relaxed modeled structure files for both the binary and ternary A-site mixtures are available with the SI.

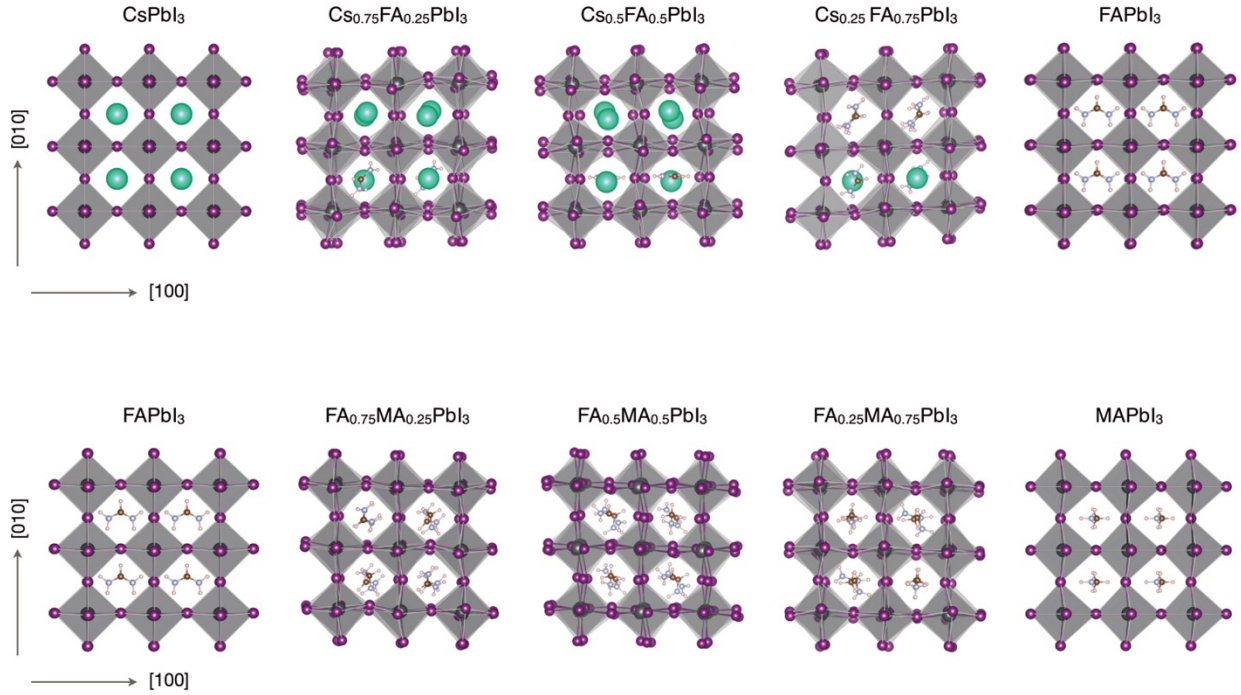

Figure S2: **Modeled relaxed mixed A-site structures.** All structures are generated using a pseudo-cubic structure with random substitution on the A-site. Lead (gray), Iodine (purple), Cs (green), Nitrogen (blue), Carbon (brown), and hydrogen (yellow) atoms are represented by spheres. The lead iodide octahedral are shaded in gray.

Density Functional Theory (DFT) calculations are performed within the projector augmented wave (PAW) method[8] as implemented in the VASP Code.[9] The Perdew Burke Ernzerhof (PBE) exchange correlation functional[10] is used within GGA. All degrees of freedom (cell shape, volume and ionic positions) are relaxed in DFT calculations and plane wave energy cutoff of 340 eV, and a Monkhorst-Pack k-point sampling[11] is used.

***Thermodynamics*.** DFT total energy calculations are performed at 0 K and entropy of each mixed A-site system is treated statistically. Equations below define how the thermodynamics variable are calculated.

Gibbs free energy of mixing (in eV/unit):

$$\Delta G_{mix} = \Delta H_{mix} - T\Delta S_{mix} \quad \text{(S1)}$$

Enthalpy of mixing (in eV/unit):

$$\Delta H_{mix} = \Delta E_{mix} \quad \text{(S2)}$$

Enthalpy of mixing is approximately given by the change in the internal energy (ΔE_{mix}), which is a valid approximation because the PΔV contribution to enthalpy of mixing is found to be negligible (in the order of 10^{-4} eV). For a given A-site concentration (x), change in internal energy is computed as:

$$\Delta E_{mix} = E_{tot}^{DFT}(mixture) - (1-x)E_{tot}^{DT}(pure\ component) - xE_{tot}^{DFT}(pure\ component) \quad \text{(S3)}$$

where, E_{tot}^{DFT} is the total energy calculated from DFT calculation.

Entropy of mixing (in eV/K-unit):

$$\Delta S_{mix} = S(mixture) - (1-x)S(pure\ component) - xS(pure\ component) \quad \text{(S4)}$$

$$\Delta S_{mix} = \Delta S_{config.} + \Delta S_{rot.} \quad \text{(S5)}$$

$$\Delta S_{config.} = S_{config.}(mixture) = -k_B[xln(x) + (1-x)ln(1-x)] \quad \text{(S6)}$$

where, k_B is the boltzmann constant.

In our calculations, we observe random orientation of both FA and MA molecules in the both FAMA and FACs cubic mixed A-site structures, which is consistent with the recent theoretical and experimental studies in these mixed A-site systems.[12–14] Therefore, ΔS_{rot} is considered to be approximately zero. This is a valid assumption because at room temperature or higher, FA molecule is free to rotate in cubic $FAPbI_3$, as well as similar observations holds true for the MA molecule in cubic and tetragonal $MAPbI_3$.[13,15] Therefore, the rotational entropy component to Gibbs free energy cancels to a large degree when comparing the cubic mixed A-site structure with respect to the cubic $FAPbI_3$, and cubic as well as tetragonal $MAPbI_3$. However, FA molecule in hexagonal $FAPbI_3$ has a preferred orientation and therefore, ΔS_{rot} contribution to Gibbs free energy for cubic FAMA (and FAMACs) mixed A-site halide perovskites at $T \leqslant 300$ K with respect to the hexagonal $FAPbI_3$ no longer cancels out. ΔS_{rot} is then calculated as:

$$\Delta S_{rot}(FA_xMA_{1-x}PbI_3) = xS_{rot}(FA) \quad \text{(S7)}$$

where, rotational entropy associated with a polyatomic molecule is given as[16]:

$$S_{rot} = k_B\left[ln\left(\frac{8\pi^2}{\sigma}\left(\frac{2\pi k_B T}{h^2}\right)^{3/2}(I_1 I_2 I_3)^{1/2}\right) + \frac{3}{2}\right] \quad \text{(S8)}$$

with σ being the symmetry number and I_1, I_2 and I_3 are moments of inertia of the molecule obtained for $FAPbI_3$ from T. Chen et al.[12]

Supplemental Data:

Table S1: Summary of the performance parameters of cells used in this study obtained from a forward and reverse sweep of 100 mV/s under 1 Sun illumination (Figure S3).

Formulation	**V_{oc} (V)**		**J_{sc} (mA/cm^2)**		**FF**		**PCE (%)**	
	Forward	Reverse	Forward	Reverse	Forward	Reverse	Forward	Reverse
$FA_{0.85}Cs_{0.15}PbI_3$	1.08	1.10	21.76	21.77	0.65	0.77	15.23	18.45
$FA_{0.758}MA_{0.152}Cs_{0.091}PbI_3$	0.93	1.04	22.20	22.23	0.45	0.72	9.34	16.50

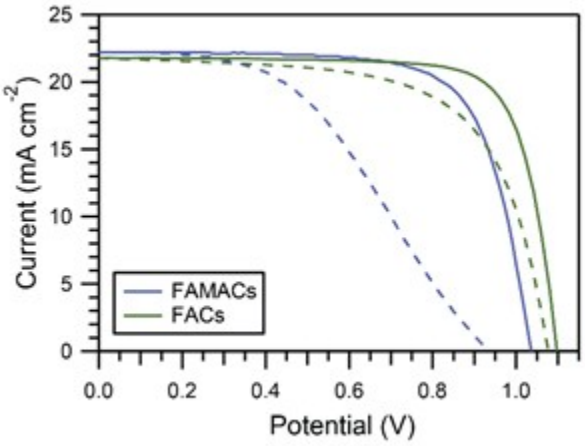

Figure S3: **1-Sun JV scans.** JV scans for $FA_{0.85}Cs_{0.15}PbI_3$ (green) and $FA_{0.758}MA_{0.152}Cs_{0.091}PbI_3$ (blue) devices measured *ex-situ* at NREL under 1 Sun illumination prior to the *in-situ* characterization at SSRL. Device parameters are summarized in table S1.

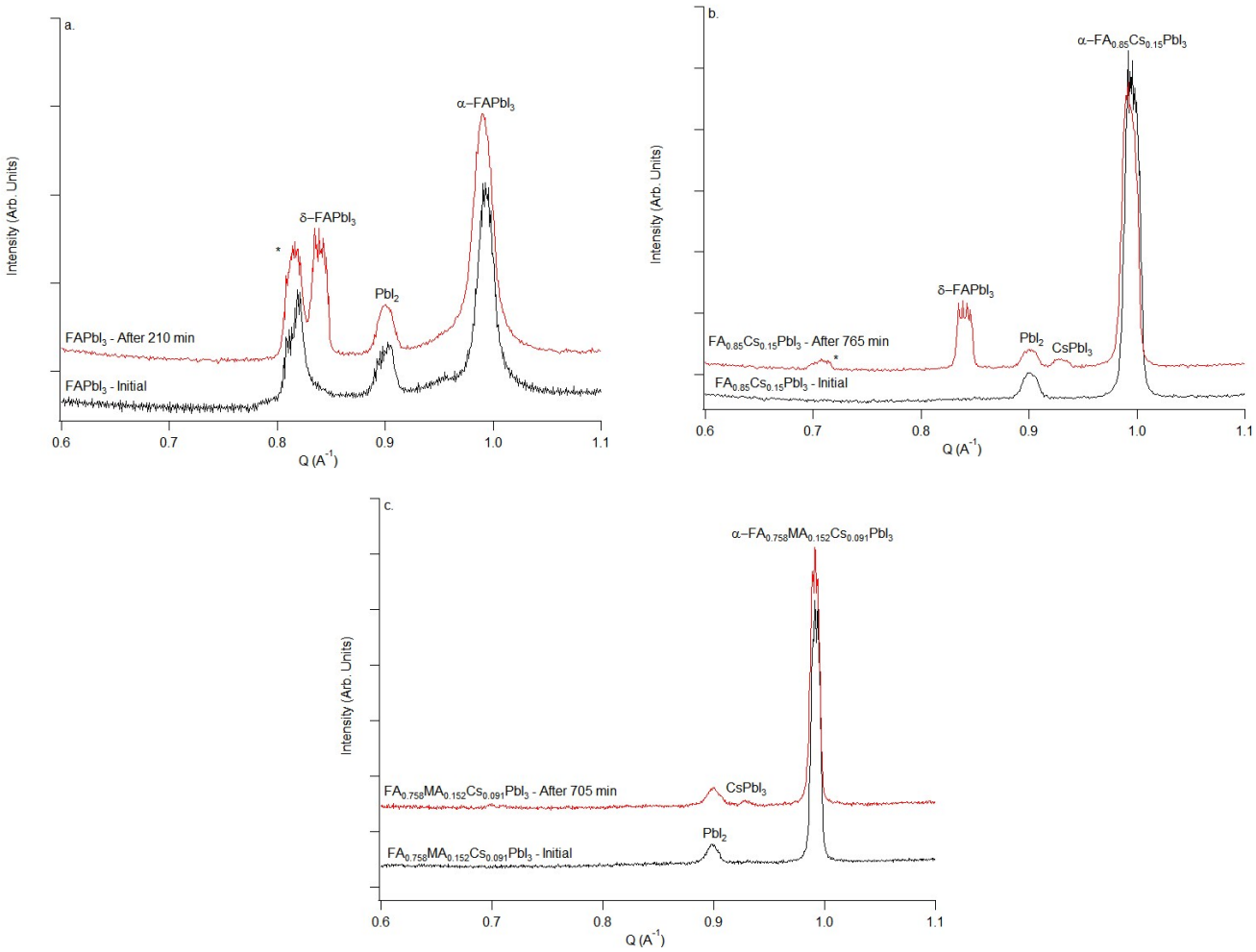

Figure S4: **2D – X-ray Diffraction of mixed A-site PSCs.** 2D X-ray diffraction profiles of the initial (black) and after cycling (red) of (a) FAPbI3, (b) $FA_{0.85}Cs_{0.15}PbI_3$, and (c) $FA_{0.758}MA_{0.152}Cs_{0.091}PbI_3$. The peak at ~ 0.8 $Å^{-1}$ (a) and 0.7 $Å^{-1}$ (b) is associated with a hydrate phase (marked by *). Scattering versus time data can be found in figure 1. Q is related to the diffraction angle (θ) and incident wavelength (λ) by $Q= (4\pi/\lambda) \sin\theta$. The X-ray wavelength used here was λ = 0.9919 Å.

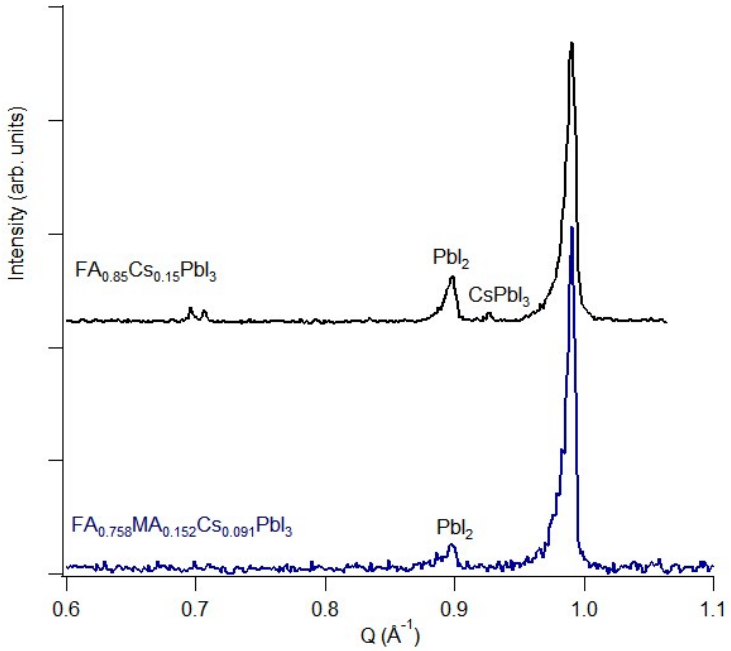

Figure S5: **Ex-situ device X-ray diffraction**. $FA_{0.85}Cs_{0.15}PbI_3$ (black) and $FA_{0.758}MA_{0.152}Cs_{0.091}PbI_3$ (Blue) devices operated off the beam-line (no X-ray exposure) and measured with a laboratory diffractometer showing comparable phase segregation to the *operando* devices. This confirms the effects seen *operando* are not X-ray beam induced.

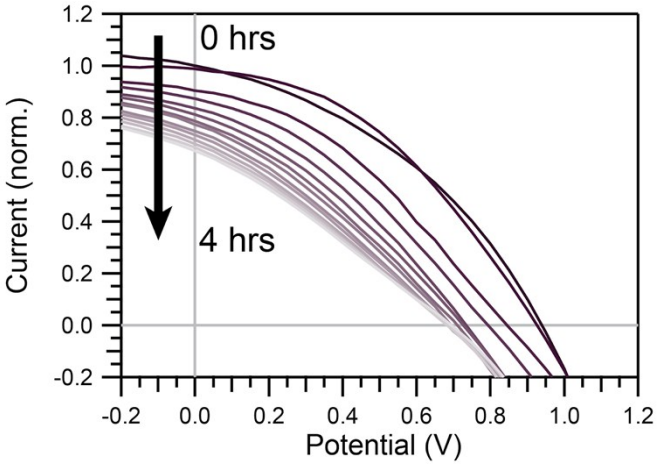

Figure S6: **Device performance degradation vs time**. Reverse scan IV curves for a $FAPbI_3$ device taken *in-situ* under the conditions described in the Experimental Methods.

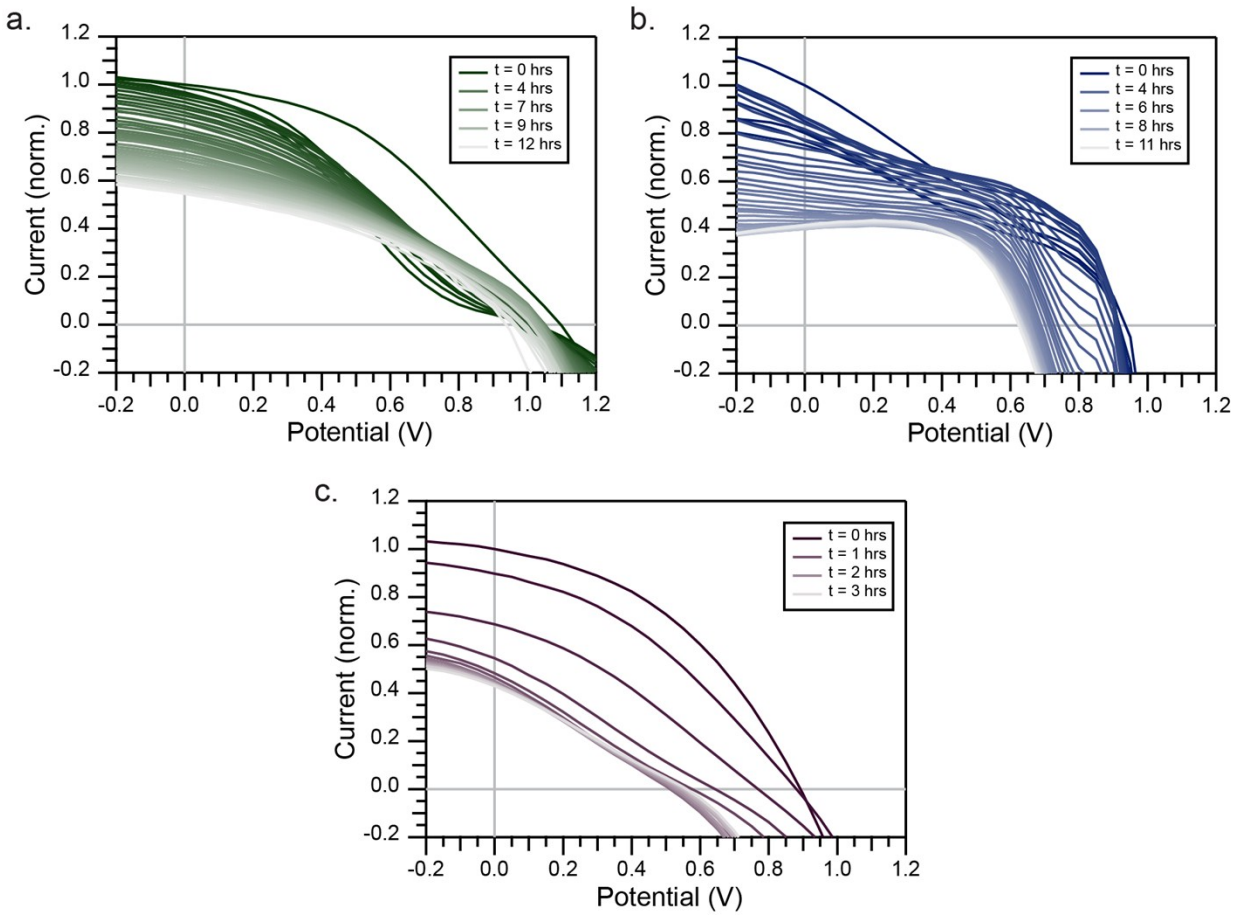

Figure S7: **Device performance degradation vs time.** Forward scan IV curves for (a) $FA_{0.85}Cs_{0.15}PbI_3$, (b) $FA_{0.758}MA_{0.152}Cs_{0.091}PbI_3$ and (c) $FAPbI_3$ devices taken *in-situ* under the conditions described in the Experimental Methods.

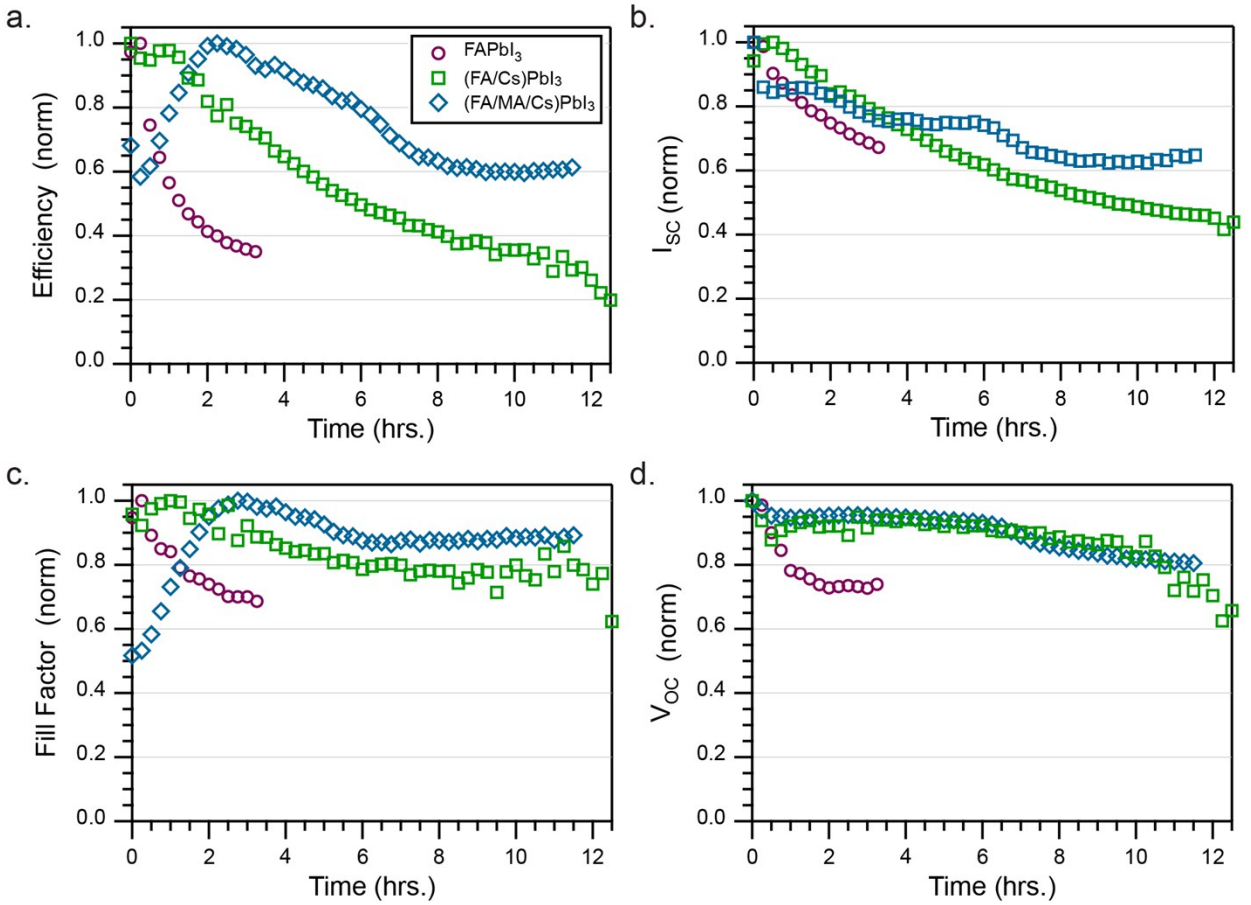

Figure S8: **Photovoltaic performance parameter versus time**. Normalized (a) Efficiency, (b) I_{sc}, (c) Fill factor, and (d) V_{oc} of $FAPbI_3$ (Purple circle), $FA_{0.85}Cs_{0.15}PbI_3$ (green square), and $FA_{0.758}MA_{0.152}Cs_{0.091}PbI_3$ (blue diamond) devices measured *in-situ* under the conditions described in the Experimental Methods.

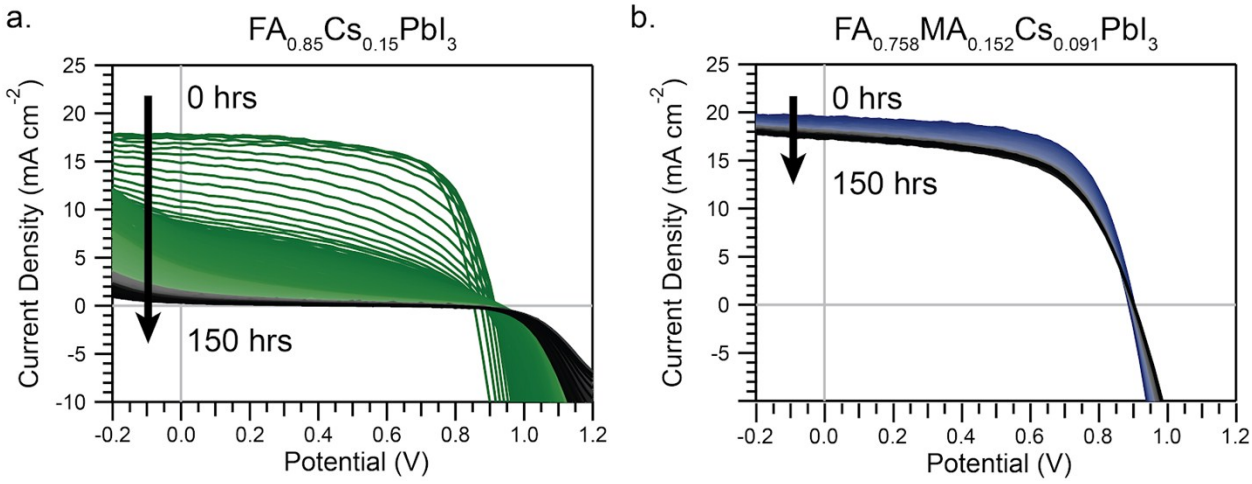

Figure S9: **Device performance degradation vs time**. Reverse scan *I-V* curves for (a) $FA_{0.85}Cs_{0.15}PbI_3$ and (b) $FA_{0.758}MA_{0.152}Cs_{0.091}PbI_3$ devices taken *ex situ* (no X-ray exposure) with a scan rate of 100mV/s. Tests were conducted under ISOS-L1 conditions as described in the

Experimental Methods. These samples were prepared with a SnO_2 electron transport layer to confirm that the A-site segregation and reduction in J_{sc} was not a result of using TiO_2.

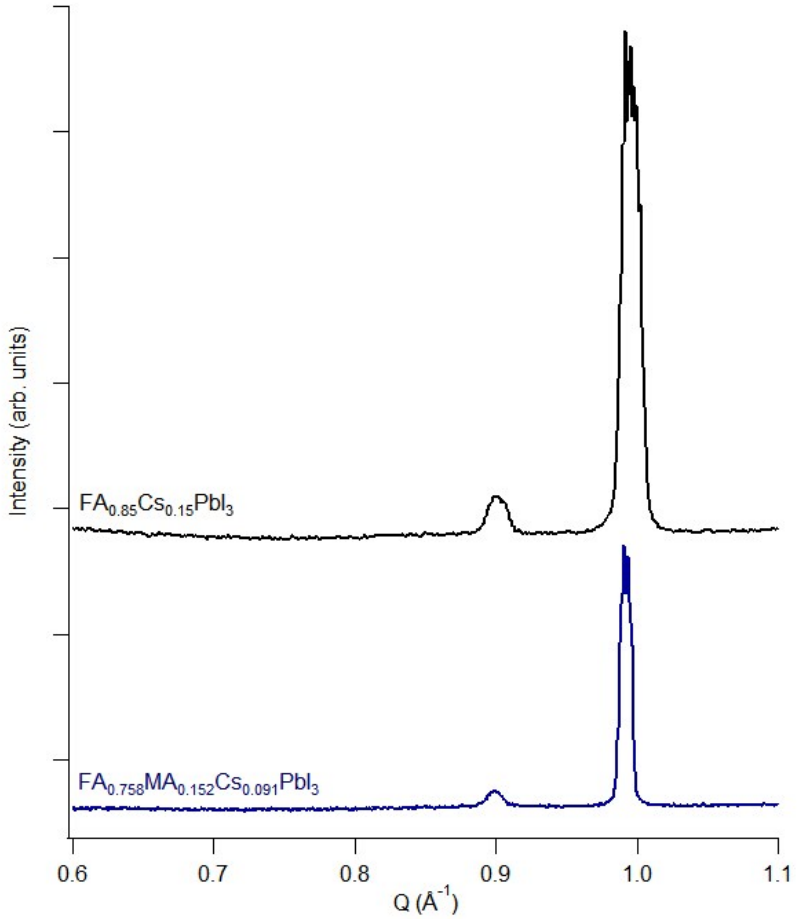

Figure S10: **Tolerance factor comparison.** XRD diffraction patterns for $FA_{0.85}Cs_{0.15}PbI_3$ (black) and $FA_{0.758}MA_{0.152}Cs_{0.091}PbI_3$ (Blue) devices. The peak at Q ~0.9 $Å^{-1}$ is attributed to PbI_2, the peak Q ~ 1.0$Å^{-1}$ is the main perovskite peak. Assuming the mixed A-site halide perovskites share the same cubic structure, the similar perovskite peak position suggests a similar lattice parameter, which would result in a comparable effective tolerance factor.

a.

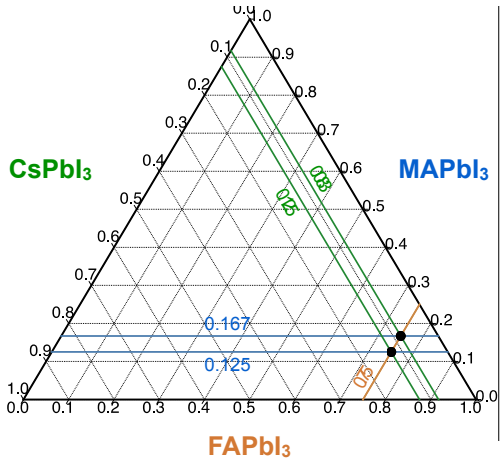

b.

Temp. (K)	Composition	Enthalpy (ΔE_{mix})	Entropy (TS_{mix})	Gibbs Free Energy (ΔG_{mix})	Pure components		
600	$FA_{0.75}MA_{0.167}Cs_{0.083}$	-0.178	0.037	-0.216	Cubic-FAPbI	Cubic-MAPbI	Cubic-CsPbI
	$FA_{0.75}MA_{0.125}Cs_{0.125}$	-0.176	0.038	-0.214	Cubic-FAPbI	Cubic-MAPbI	Cubic-CsPbI
300	$FA_{0.75}MA_{0.167}Cs_{0.083}$	-0.165	0.019	-0.184	Cubic-FAPbI	Cubic-MAPbI	Ortho-CsPbI
	$FA_{0.75}MA_{0.125}Cs_{0.125}$	-0.156	0.019	-0.175	Cubic-FAPbI	Cubic-MAPbI	Ortho-CsPbI
300	$FA_{0.75}MA_{0.167}Cs_{0.083}$	0.136	0.238	-0.102	Hexa-FAPbI	Tetra-MAPbI	Ortho-CsPbI
	$FA_{0.75}MA_{0.125}Cs_{0.125}$	0.142	0.238	-0.096	Hexa-FAPbI	Tetra-MAPbI	Ortho-CsPbI

Figure S11: **DFT calculations of ternary mixed A-site halide perovskites**. (a) Composition of the ternary mixed A-site halide perovskite indicated on a Gibbs triangle with corners representing pure end members. (b) Calculated enthapy, entropy and Gibbs free energy of mixing in eV/unit.

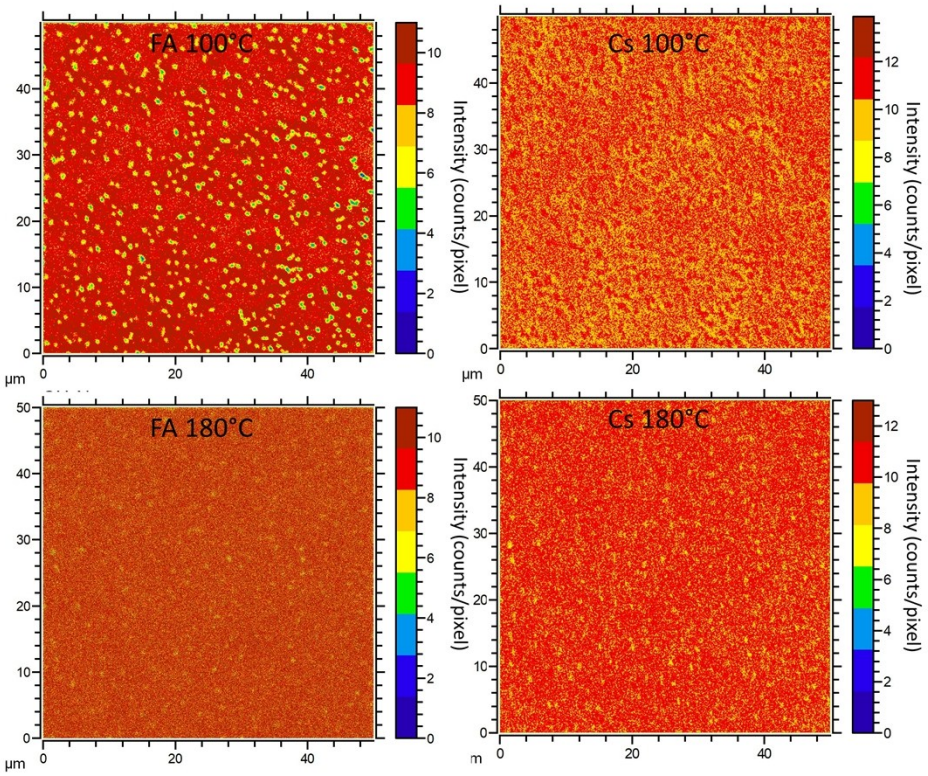

Figure S12. **TOF-SIMS of $FA_{0.7}Cs_{0.3}PbI_3$ exposed to different annealing temperatures.** TOF-SIMS mapping of FA, and Cs in $FA_{0.7}Cs_{0.3}PbI_3$ devices after annealing at 100°C and 180°C. At lower temperature the films are phase segregated, upon higher thermal treatment the films are much more homogeneous, consistent with the presented theory and *in situ* XRD.

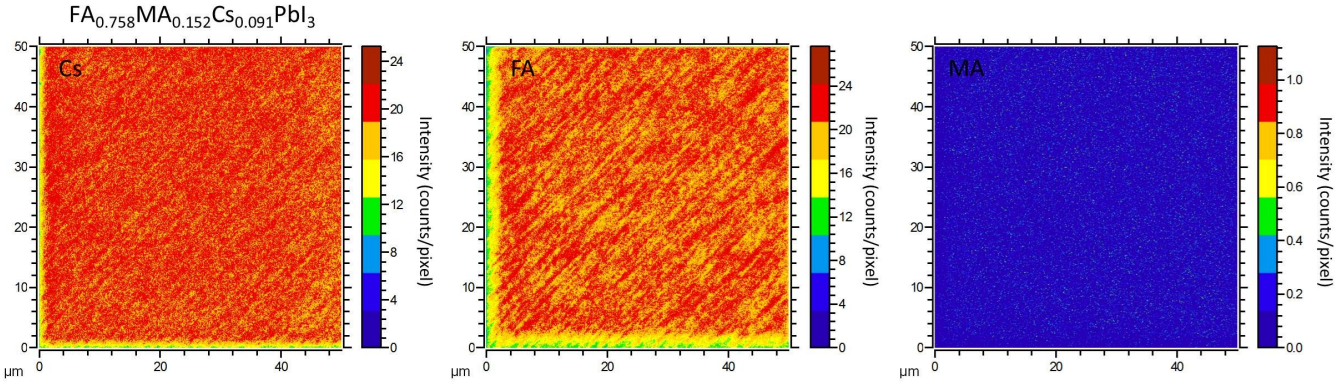

Figure S12. **TOF-SIMS of $FA_{0.75}MA_{0.167}Cs_{0.083}PbI_3$.** TOF-SIMS mapping of FA, MA and Cs in an annealed $FA_{0.75}MA_{0.167}Cs_{0.083}$ film. The apparent drop in intensity near the edges of the image is a measurement artifact. Due to the long integration time of the measurement a non-negligible amount of material is removed by the SIMS primary ion beam, which can result in crater edge effects at the boundaries of the analysis area as seen here.

Supplemental References:

1 L. T. Schelhas, J. A. Christians, J. J. Berry, M. F. Toney, C. J. Tassone, J. M. Luther and K. H. Stone, *ACS Energy Lett.*, 2016, **1**, 1007–1012.

2 B. H. Toby and R. B. Von Dreele, *J. Appl. Crystallogr.*, 2013, **46**, 544–549.

3 S. Harvey, Z. Li, J. A. Christians, K. Zhu, J. M. Luther and J. J. Berry, *ACS Appl. Mater. Interfaces*, , DOI:10.1021/acsami.8b07937.

4 C. C. Stoumpos, C. D. Malliakas and M. G. Kanatzidis, *Inorg. Chem.*, 2013, **52**, 9019–9038.

5 A. Zunger, S.-H. Wei, L. G. Ferreira and J. E. Bernard, *Phys. Rev. Lett.*, 1990, **96**, 312–318.

6 A. Van de Walle, M. Asta and G. Ceder, *Calphad Comput. Coupling Phase Diagrams Thermochem.*, 2002, **26**, 539–553.

7 A. Van De Walle, P. Tiwary, M. De Jong, D. L. Olmsted, M. Asta, A. Dick, D. Shin, Y. Wang, L. Q. Chen and Z. K. Liu, *Calphad Comput. Coupling Phase Diagrams Thermochem.*, 2013, **42**, 13–18.

8 P. E. Blöchl, *Phys. Rev. B*, 1994, **50**, 17953–17979.

9 G. Kresse and J. Furthmüller, *Comput. Mater. Sci.*, 1996, **6**, 15–50.

10 J. P. Perdew, K. Burke and M. Ernzerhof, *Phys. Rev. Lett.*, 1996, **77**, 3865–3868.

11 H. J. Monkhorst and J. D. Pack, *Phys. Rev. B*, 1977, **16**, 1748–1749.

12 T. Chen, B. J. Foley, C. Park, C. M. Brown, L. W. Harriger, J. Lee, J. Ruff, M. Yoon, J. J. Choi and S. H. Lee, *Sci. Adv.*, 2016, **2**, 1–7.

13 D. H. Fabini, T. A. Siaw, C. C. Stoumpos, G. Laurita, D. Olds, K. Page, J. G. Hu, M. G. Kanatzidis, S. Han and R. Seshadri, *J. Am. Chem. Soc.*, 2017, **139**, 16875–16884.

14 M. T. Weller, O. J. Weber, J. M. Frost and A. Walsh, *J. Phys. Chem. Lett.*, 2015, **6**, 3209–3212.

15 W. A. Saidi and J. J. Choi, *J. Chem. Phys.*, , DOI:10.1063/1.4964094.

16 S. Glasstone, *Thermodynamics for Chemists*, Read Books, 2007.